ASME Journal of Solar Energy Engineering
Online journal at:
https://asmedigitalcollection.asme.org/solarenergyengineering

Habilou Ouro-Koura[1]
Department of Mechanical, Aerospace, and Nuclear Engineering,
Rensselaer Polytechnic Institute,
Troy, NY 12180;
Energy and Environment Directorate,
Pacific Northwest National Laboratory,
Richland, WA 99354
e-mail: habilou.ourokoura@pnnl.gov

Hyunjun Jung
Energy and Environment Directorate,
Pacific Northwest National Laboratory,
Richland, WA 99354
e-mail: hyunjun.jung@pnnl.gov

Diana-Andra Borca-Tasciuc
Department of Mechanical, Aerospace, and Nuclear Engineering,
Rensselaer Polytechnic Institute,
Troy, NY 12180
e-mail: borcad@rpi.edu

Andrea E. Copping
Energy and Environment Directorate,
Pacific Northwest National Laboratory,
Richland, WA 99354
e-mail: andrea.copping@pnnl.gov

Zhiqun (Daniel) Deng
Energy and Environment Directorate,
Pacific Northwest National Laboratory,
Richland, WA 99354;
Department of Naval Architecture and Marine Engineering,
University of Michigan,
Ann Arbor, MI 48109
e-mail: zhiqun.deng@pnnl.gov

Modeling and Optimization of a Phase Change Material-Based Ocean Thermal Energy Harvester for Powering Uncrewed Underwater Vehicles

As oceans cover over 70% of the planet's surface, they represent a large reservoir of resources that remain vastly untapped. Uncrewed underwater vehicles (UUVs) are becoming a key technology for ocean exploration. Ocean thermal gradient is a permanent and reliable energy source that can be used to power UUVs using phase change material (PCM)-based thermal engines. When using PCM-based thermal engines to power UUVs, there are different energy conversion stages: thermal, hydraulic, kinetic, and electrical, dependent on a wide variety of parameters. Thus, optimization of the overall energy conversion is still a challenge for powering the increasing energy demanding UUVs for long missions. The goal of this study is to propose a PCM-based ocean thermal energy harvesting system for powering float-type UUVs such as the SOLO-II float. This reduces the cost of battery replacement and expands the float's mission time. For this purpose, we developed a theoretical model consisting of hydraulic and electrical systems, designed to provide the electrical power needed by the UUV. The hydraulic and electrical systems are implemented using MATLAB/SIMULINK. Parameter values from the literature and an accumulator size of 3.78 L are used. The mass of PCM calculated for the energy harvesting system is 5.73 kg, providing a theoretical volume change of 0.78 L. Varying the value of the electrical load connected to the electrical generator, the developed model can, theoretically, provide 13.66 kJ of electrical energy, which is more than 1.5 times the energy requirement per cycle for the SOLO-II float. [DOI: 10.1115/1.4065553]

Keywords: simulation, energy, efficiency, uncrewed underwater vehicles, phase change material, optimization, clean energy, renewable, system

1 Introduction

Oceans are an important climate regulator [1] and hold enormous natural resources such as water, minerals (manganese nodules), and metal deposits (cobalt-rich ferromanganese, sulfides, nickel, titanium, molybdenum, platinum, and rare earth elements) [2]. While portions of the coastal oceans have been inventoried and natural resources such as marine animals, habitats, seafloor minerals, and constituents of seawater are reasonably well understood, there are insufficient data with which to accurately validate models of climate change [3]. Similarly, the bathymetry and sediment content of the seafloor are not well studied away from the land [4]. Scientific campaigns that will map the seafloor; assess changes in the temperature and salinity gradients in the oceans driven by climate change, as well as marine energy from waves and underwater currents; explore and discover new species of marine biota from bacteria to the apex of the food chain; and inventory the geochemistry of the deep sea will all require power to propel autonomous underwater vehicles (AUVs) and fixed observation platforms. These data are needed to understand ocean climate patterns and to provide the necessary data needed to inform the emerging Blue Economy [5].

Modern climate models rely heavily on experimental data and scientists need to collect vast amounts of critical information to adjust them to accurately predict the earth's climate change [6].

[1]Corresponding author.

Contributed by the Solar Energy Division of ASME for publication in the JOURNAL OF SOLAR ENERGY ENGINEERING: INCLUDING WIND ENERGY AND BUILDING ENERGY CONSERVATION. Manuscript received July 31, 2023; final manuscript received May 4, 2024; published online June 13, 2024. Assoc. Editor: Julia Haltiwanger Nicodemus.

Examples of such key information include ice sheet melting rate especially at Polar Regions, yearly average ocean temperature, salinity, pH, dissolved oxygen, and acidity at different locations around the globe [7]. There is also a need to add biogeochemical information to understand the status of the world's oceans [7]. Methods used to collect this data include having ocean observatory stations (buoys), satellites, observation ships, and oceangoing manned or uncrewed underwater vehicles (UUVs) (remote operated vehicles, gliders, as well as floats) [8].

Uncrewed underwater vehicles are an excellent and cost-effective approach to accomplishing underwater tasks since they can withstand the harsh environment of the ocean depth (high pressure, cold temperature), they do not require a human onboard, and can stay under the sea for a long time. However, UUVs' mission duration and range are hampered by their existing energy sources, typically batteries, because of their limited stored energy. Batteries are also potential ocean pollution hazards when damaged [9]. To address these shortcomings, self-powered UUVs are currently being explored investigating three main energy sources: solar, kinetic, and thermal.

Solar powered autonomous underwater vehicle (SAUV II) is a pioneer to use solar energy to charge its batteries [10]. However, the SAUV II can only charge its batteries during the daytime. Kinetic or wave energy is only available at the surface and may not be suitable for underwater exploring vehicles [11].

Ocean thermal energy mainly comes from the sun and can be used to generate electricity [12]. Ocean thermal gradient is a strong candidate for powering UUVs. The thermal gradients in the ocean are small but stable and performance of energy-harvesting UUVs including re-charging times can be predicted with more accuracy. Phase change material (PCM)-based ocean thermal energy harvesters have been demonstrated for powering UUVs, and practical systems have emerged such as the Seatrec SL1 and the most recent infiniTE^{TM} float. PCMs are used in other practical applications such as heat energy storage [13,14], and in hybrid energy harvesting systems [15].

These systems use a thermal engine, as described in Sec. 3.1, to harvest the ocean thermal energy between the temperature difference of the warm sea surface waters and the cold deep waters. The energy harvested by the thermal engine is usually stored in the form of a pressurized hydraulic fluid and is mainly used in two ways [9]. First, the stored energy is used for motion such as for buoyancy change of the underwater vehicle [16,17]. Second, the stored energy is converted into electrical energy to power sensors, communication systems, as well as propulsion, as in Refs. [18–20], or a combination of those two usages, e.g., in Ref. [21].

SLOCUM thermal glider, PETREL, SOLO-TREC, OTEC-PCM, and Navis-SL1, are all examples of UUVs that use PCM-based thermal energy harvesting technology [9]. Other thermal energy harvesting methods based on ocean thermal energy conversion (OTEC), and shape memory alloys are only at the conceptual design phase and have not been successfully integrated into UUVs [9].

Researchers are still working to improve the performance of PCM-based energy harvesters by increasing their overall energy conversion efficiency. For example, Ma et al. [22] studied the effect of residual air inside a thermal engine and air solubility within the PCM on the energy storage of a PCM-based thermal energy harvesting system. Their prototype system could store 2.48 kJ of hydraulic energy per profile during sea trial. Liu et al. developed a theoretical analysis of the heat transfer and a parametric study of the energy storage of a piston-type PCM-based thermal engine. Concurrently, studies of the PCM and its performance optimization during phase transitions have also been conducted [23,24]. Wang et al. proposed an efficiency model of the electrical generation system and performed a parametric study of the main parameters affecting the energy conversion efficiency [18].

While PCM-based energy harvesters are currently commercialized, they are still plagued by a very low energy conversion efficiency [9]. The state-of-the-art prototype (OTEC-PCM) based on a developed mathematical model showed an average total efficiency of 0.396% [18]. As a reference, this value is far from the maximum theoretical value from the Carnot efficiency limit, which is ~7.9% under the same temperature difference. More recently, Zhang et al. [20] developed a prototype of a modular ocean thermal energy harvester for electrical energy storage. Their prototype generated, after sea trials, an average electrical energy of 1.368 Wh. Compared to the thermoelectric generators, which have an average efficiency of 0.1% for ocean thermal gradient applications [9], the PCM-based UUVs have a high total average efficiency of energy conversion from ocean thermal gradient to electricity. Despite these studies, PCM-based ocean energy harvesting technology still needs improvements to be widely incorporated in UUVs to accomplish Henry Stommel's vision of having a vast array of marine underwater vehicles independently powered by the ocean [25]. Emerging underwater vehicles require an increasing amount of electrical energy which can range (for average energy consumption vehicles) from 5.4 kJ (1.5 Wh) for the low-power Seaglider (sg564) to 53.2 kJ (14.8 Wh) for the Petrel-II Glider [26]. This energy requirement is used to power the propulsion, control, and communication systems as well as the growing suite of sensors onboard.

Since 1999, the Argo program, an international collaboration of researchers, has used floats for collecting information such as temperature, pressure, salinity, oxygen, and pH from the depths of Earth's oceans. Those floats (over 3900) have a lifetime of approximately 5 years and are limited by the duration of the lithium batteries powering the different sensors and the pump required for buoyancy change [27]. Since the batteries have finite energy stored, they are a major limitation for the mission duration of the floats; therefore, not using them as the major power source will greatly increase the lifetime of the floats and significantly reduce their overall mission cost. Thus, an ocean thermal gradient energy harvesting system which continuously provides the electrical energy necessary to recharge batteries, or any onboard electrical storage system such as supercapacitors, is essential for cost-effective and long-term duration missions. For instance, the thermal engine will be used to gradually collect and convert the ocean thermal energy into mechanical energy during the profiling cycle of the float. The mechanical energy can quickly be converted into electrical energy for recharging the float's electrical power bank, which will power the float for the following cycle. In this context, this work proposes a simplified modeling and optimization process for a system, which during one profiling cycle of the float, will be able to collect the ocean thermal energy and generate enough electrical energy. This electrical energy will be used to recharge the onboard electrical power source for the subsequent profiling cycle, for one of the widely used floats of the Argo program, the SOLO-II.

Table 1 Standard commercially available bladder-type accumulators [33]

Accumulator size	Maximum gas volume	Maximum pressure
1 gallon (3.79 L)	214 in.^{3} (3.51 L)	6000 psi (41.37 MPa)
1.5 gallon (5.68 L)	328 in.^{3} (5.37 L)	3000 psi (20.68 MPa)
2.5 gallon (9.46 L)	536 in.^{3} (8.78 L)	6000 psi (41.37 MPa)
5 gallon (18.93 L)	1106 in.^{3} (18.12 L)	6000 psi (41.37 MPa)

2 SOLO-II Float

Profiling floats are scientific instruments characterized by their vertical motion underwater and horizontal drifting by ocean currents. Floats can be in different shapes and are traditionally cylindrical or bottle-shaped. Profiling floats move underwater by changing their buoyancy; therefore, they generally require an external bladder which increases its volume for ascent and decreases its volume for descent. To perform this operation, a high-pressure hydraulic pump is generally required. In general, floats are less energy-demanding compared to other UUVs such as gliders, or other AUVs; thus,

they have an extended mission lifetime of 5 or more years which is limited by the capacity of their internal batteries. In spite of their relatively smaller size, floats can carry many sensors due to their low energy consumption for propulsion and control systems [27]. SOLO-II represents a modern float with a volume of around 18 L designed by the Scripps Institute of Oceanography (SIO) and deployed by Woods Hole Oceanographic Institution (WHOI) since 2012 [27,28]. SOLO-II is composed mainly of an antenna that most commonly uses the global positioning system (GPS) for the location of the float and the iridium satellites network for data transfer; a conductivity, temperature, and depth sensor; a controller; hydraulic pump; an external bladder; and lithium batteries [27].

SOLO-II float normally has a 10-day profiling cycle during which the float descends to a predetermined depth, typically 1000 m, where it drifts horizontally with the ocean currents while taking measurements with the onboard sensors, for approximately 9 days. Then, the float may descend to its maximum depth (~2000 m) after which it ascends to the surface while taking measurements with its sensors. At the surface, it sits for about an hour to send the collected data to the iridium satellite network and receive additional tasks, as well as communicating with the GPS for its location [27]. During a profiling cycle, the total energy consumption of the SOLO II-float is estimated at 8.1 kJ over the 10-day cycling time [29]. This energy requirement will be used as a baseline electrical energy requirement for the model and optimization of the ocean thermal energy harvesting system described here.

3 Model Description

3.1 Thermal Engine. The main function of the thermal engine of a PCM-based ocean thermal energy harvesting system is to convert the ocean thermal energy into usable mechanical energy. This is accomplished by using a phase change material that expands and contracts in volume producing mechanical work on a working fluid. This mechanical work is typically stored in a hydraulic accumulator in the form of high-pressure potential hydraulic energy. When the PCM is cooled, it contracts; and then melts and expands as the temperature rises, taking more volume and pressurizing the hydraulic fluid inside a pressure vessel [9,30]. The pressurized hydraulic oil can be stored as a potential hydraulic energy source or used to drive a hydraulic motor, which in turn can drive a generator to produce electricity. This process can be used cyclically to continuously provide the power needed for a UUV. Usually in the form of a cylinder, a thermal engine is composed of an external shell made from a high heat conductive material, a flexible inner bladder that contains a working fluid, with the PCM in between the metal shell and the bladder [30].

For the example of a SOLO-II float, when it descends to 1000 m or more, the temperature of water will be ~5 °C, and the PCM inside the pressure vessel will contract. When the float travels upward to the warm surface waters (~25 °C), the PCM will expand and pressurize the working fluid, providing the mechanical energy needed. This energy is stored in a hydraulic accumulator.

For simplicity, the structure of the thermal engine is ignored, and the thermal engine model in this paper is limited to the mass of PCM needed to obtain a volume change inside a hydraulic accumulator to provide the necessary hydraulic energy.

As from previous studies [18,30,31], hexadecane is chosen among other paraffin PCMs for its high volume change from solid to liquid phases (11.77%, theoretical), safety for the marine environment, and a melting temperature of 18.2 °C that spans the temperature change between the deep cold and warm surface ocean waters. To determine the mass of hexadecane needed, the energy conversion efficiency values are taken from the values shown in Fig. 2 of Ref. [18]. Using the hydraulic-to-kinetic energy conversion efficiency $\eta_1 = 50\%$, and the kinetic-to-electric efficiency $\eta_2 = 60\%$, the total hydraulic-to-electric energy conversion efficiency, η_{total}, is given by Eq. (1), equating to 30%.

$$\eta_{\text{total}} = \eta_1 \times \eta_2 \tag{1}$$

The hydraulic energy required to meet the 8.1 kJ electrical energy of the SOLO-II is calculated as

$$E_{\text{hydraulic}} = \frac{E_{\text{electrical}}}{\eta_{\text{total}}} \tag{2}$$

$E_{\text{hydraulic}}$ needed is 27 kJ.

Following a polytropic and adiabatic process, the energy stored inside a hydraulic accumulator is given by Eq. (3) [32].

$$E_{\text{hydraulic}} = \frac{P_{\text{initial}} \times V_{\text{initial}}}{n-1}\left[\left(\frac{P_{\text{initial}}}{P_{\max}}\right)^{\frac{1-n}{n}} - 1\right] \tag{3}$$

where $n = 1.4$ for nitrogen gas.

The size (V_{initial}) and the initial pre-charge pressure (P_{initial}) of the hydraulic accumulator play a significant role in optimizing the hydraulic energy. Different sizes of commercially available bladder-type accumulators (as in OTEC-PCM), which meet the ASME standard for pressure vessels, are used to calculate P_{initial} from Eq. (3) to get the optimal accumulator size (Table 1).

As shown in Fig. 1, P_{initial} increases with an increase in the accumulator volume, except for the nominal 1.5-gallon accumulator, due to its lower maximum pressure of 20.68 MPa (3000 psi). When the accumulator size increases from 1-gallon to 2.5, and to 5-gallon, P_{initial} increases from 29 MPa (4218.84 psi) to 39.2 MPa (5691.75 psi). As discussed in Ref. [34], a high-pressure differential enhances the overall efficiency of the energy conversion system under consideration in this paper, therefore a high P_{initial} is needed. Practically, a larger accumulator size may be too large in volume and too heavy for an energy conversion system, therefore, for this study, a 1-gallon accumulator is used. It has also been discussed by Hou et al. [35] that current thermal engines work at lower pressures than the maximum pressure a paraffin wax PCM can provide, which can be upto 90 MPa (13053.4 psi). Therefore, this model provides a maximum pressure of 41.4 MPa (6000 psi), which can be achieved by the PCM.

Knowing P_{initial} and the size of the accumulator, the necessary volume change of the nitrogen gas within the accumulator using Eq. (4*b*) and the corresponding mass of hexadecane can be calculated.

$$\Delta V_{N_2} = V_{\text{initial}} - V_{\text{final}} \tag{4a}$$

$$\Delta V_{N_2} = V_{\text{initial}}\left[1 - \left(\frac{P_{\text{initial}}}{P_{\max}}\right)^{\frac{1}{n}}\right] \tag{4b}$$

The calculated value of ΔV_{N_2} is 47.6 in.^{3} (0.78 L). Assuming the same volume change for the PCM, the mass of hexadecane, m_{PCM}, is determined using Eq. (5).

$$m_{\text{PCM}} = \Delta V_{N_2} \times \frac{\rho_{\text{PCM(s)}}}{11.77\%} \tag{5}$$

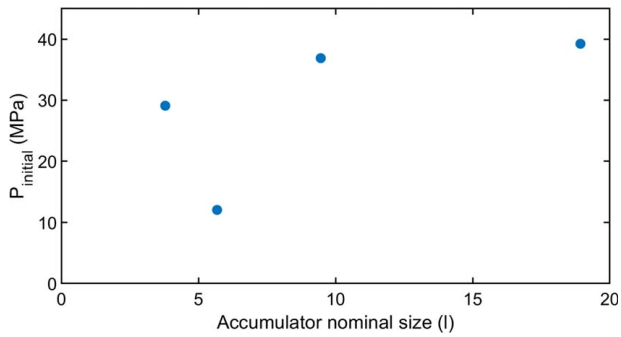

Fig. 1 Initial pressure required in the accumulator with different accumulator sizes given in Table 1

where $\rho_{PCM(s)}$ is the density of hexadecane in the solid state, which is 864 kg/m^3 [31]. The mass of PCM, m_{PCM}, needed for the thermal energy harvester is 5.73 kg.

3.2 Hydraulic and Electrical Systems. The traditional energy conversion system for electrical generation PCM-based thermal energy harvesters is composed of a thermal engine, a hydraulic accumulator, a hydraulic motor, and an electrical generator. In this work, the pressure generated by the thermal engine is substituted with a pressure source for simplification (Fig. 2). This simplified model shows a pressure source that pushes a hydraulic fluid inside the accumulator. A pressure relief valve diverts the hydraulic oil into a reservoir once the maximum pressure is reached inside the accumulator. The pressure relief valve is mounted between the pressure source and a check valve; the check valve prevents the oil in the accumulator from returning to the pressure source. An orifice valve replacing a solenoid valve is initially closed and is placed to the right of the accumulator. When the pressure inside the accumulator reaches its maximum value, the solenoid valve opens. The pressurized hydraulic oil flows through a hydraulic motor which is directly coupled to a generator. The hydraulic oil flow generates the rotation of the hydraulic motor's shaft due to the pressure difference at its inlet and outlet. The rotation of the hydraulic motor spins the electrical generator which is connected to an electrical load to dissipate the electrical power. The hydraulic oil returns to a reservoir at atmospheric pressure. The choice of hydraulic oil, the hydraulic motor, and the electrical generator are important for an efficient hydraulic-to-kinetic and kinetic-to-electric energy conversion.

For the choice of hydraulic oil, Wang et al. concluded in their work that a low-viscosity oil increases the overall efficiency of the system [18]. This is practical, as the low-viscosity hydraulic oil reduces the viscous losses inside the hydraulic line. Nevertheless, the viscosity of the hydraulic oil also affects the efficiency of the hydraulic motor, mainly the mechanical loss due to friction and lack of lubrication [36], and the volumetric loss due to internal leakage of the hydraulic motor. Generally, hydraulic motor manufacturers provide the optimal hydraulic oil viscosity for a specific motor. In this model, a hydraulic oil with a viscosity of 26 cSt and density of 866 kg/m^3 is used as for the OTEC-PCM, with a bulk modulus value of 0.8 GPa. Table 2 summarizes the main parameters of the components used in the MATLAB/SIMULINK model shown in Fig. 3. The pipe connecting the different components in the hydraulic circuit has an internal diameter of 3 mm, as for the OTEC-PCM. For the electrical generator, a DC motor is used to avoid the losses due to the use of an electrical rectifier as is the case when an AC motor is used. A Maxon permanent magnet DC motor (Model No. 388986) is used to model the electrical generator for its high efficiency (85%). As discussed in Ref. [34], the electrical load current which can be controlled with the resistance value affects the efficiency of the system. The resistance or electrical load substitutes for the external load connected to the generator which traditionally consists of a power management circuit and the electrical energy storage device such as batteries or supercapacitors. Finally, an optimization of the electrical load resistance value is performed for an efficient electrical energy generation.

Table 2 Parameters of the main components in the simulation

Component	Parameter	Value
Accumulator	Volume	3.51 L
	Pre-charge pressure	29 MPa
Hydraulic motor	Displacement	0.4 cm^3/rev
	Nominal angular velocity	2000 rpm
	Nominal pressure	14 MPa
	Volumetric efficiency at nominal conditions	0.92
	No-load torque	3 mN · m
Check valve	Cracking pressure	2 kPa
Hydraulic pipeline	Length	10 cm
	Diameter	0.3 cm
DC motor	Armature resistance	0.174 Ω
	Armature inductance	0.076 mH
	Voltage	36 V
	No-load current	0.437 A

The hydraulic and electrical energy systems are modeled in MATLAB/SIMULINK (MATLAB 2023b) (Fig. 3). The hydraulic circuit is modeled in the isothermal liquid domain (IL) as the working fluid's temperature is assumed to be constant throughout the working cycle. The hydraulic oil is considered incompressible. The cavitation effect and fluid inertia are ignored. The opening/closing dynamics of the different valves in the model are also ignored. Theoretical equations for the components are documented in MATLAB; therefore, they are omitted here.

The pressure and volume inside the hydraulic accumulator are modeled using the polytropic process, given by Eq. (6)

$$P_G V_G^n = P_{initial} V_{initial}^n \tag{6}$$

The hydraulic motor is modeled using analytical leakage and friction parameterization. The leakage flowrate, $\dot{m}_{leak}$, is given by [37]

$$\dot{m}_{leak} = K \rho_{avg} \Delta P \tag{7}$$

where K is the Hagen–Poiseuille's coefficient, ρ_{avg} is the average hydraulic fluid density, and ΔP is the pressure difference at the hydraulic motor's ports.

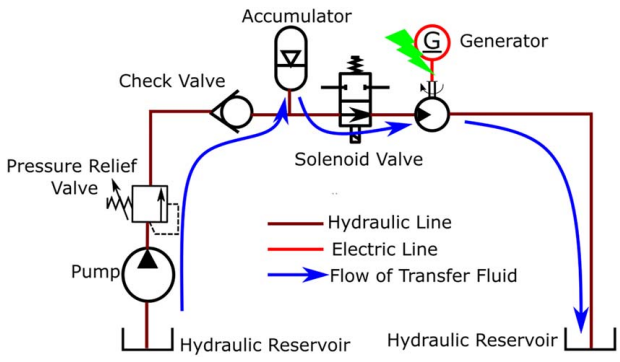

Fig. 2 Schematic of the hydraulic and electrical systems

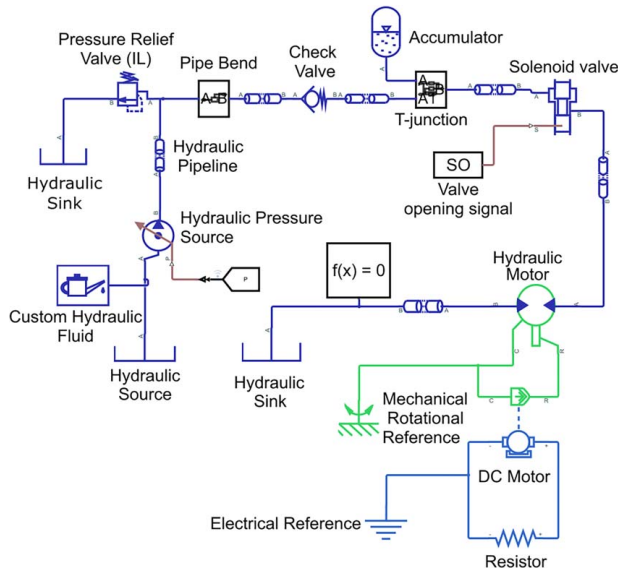

Fig. 3 Hydraulic and electrical model in MATLAB/SIMULINK

The theoretical model for the mechanical and volumetric losses in a hydraulic motor is discussed in Ref. [18]. The back-emf, v, across the DC generator is given by [38]

$$v = k_v \times \omega \tag{8}$$

where k_v is the back-emf constant and ω, the angular velocity of the generator's shaft. Reciprocally, with different load currents, the generator generates a torque $\tau_{electrical}$ given by

$$\tau_{electrical} = k_t \times i \tag{9}$$

where k_t is the torque constant and i is the current.

The power $p_{electrical}$ generated by the generator is given by

$$p_{electrical} = v \times i \tag{10}$$

From the model, the energy from the accumulator is calculated as

$$E_{Acc} = \int_{T_0}^{T_f} P_{Acc} q_{Acc} dt \tag{11}$$

where P_{Acc} and q_{Acc} are respectively the instantaneous pressure and volumetric flowrate inside the accumulator. T_0 and T_f are the initial and final time of the process, respectively.

The kinetic energy from the hydraulic motor is given by

$$E_{kinetic} = \int_{T_0}^{T_f} \tau_m \omega_m dt \tag{12}$$

where τ_m and ω_m are the torque and speed generated by the hydraulic motor, respectively.

Equation (13) gives the electrical energy dissipated by the electrical load

$$E_{electrical} = \int_{T_0}^{T_f} Ri^2 dt \tag{13}$$

The energy conversion efficiencies are given by

$$\eta_1 = \frac{E_{kinetic}}{E_{Acc}} \tag{14}$$

$$\eta_2 = \frac{E_{electrical}}{E_{kinetic}} \tag{15}$$

The total efficiency of the system can be calculated using Eq. (1).

4 Results and Discussion

Once the model was built in MATLAB/SIMULINK, an optimization process was performed to determine the optimal electrical load for maximum electrical energy output. Thus, different resistance values for the electrical load were entered and the electrical energy was calculated from the model. Figure 4 shows the variation of the electrical energy as a function of the electrical load resistance values. Due to the maximum practical power limit of the electrical generator, very small resistance values are selected, and the maximum resistance value is set to 0.4 Ω.

The energy values are calculated from the time the solenoid valve is opened (T_0) to the time (T_f) where all the hydraulic oil has flown out of the accumulator.

Figure 4 shows that as the value of the resistive load increases from 0.05 Ω to 0.4 Ω, the electrical energy generated also increases from 3.3 kJ to 13.66 kJ. This is due to the fact that as the load value increases, the electrical current decreases, decreasing the torque on the motor shaft. At low resistance values and high torque, the DC generator is not efficient. At 0.2 Ω, the calculated electrical energy generated by the generator is 9.5 kJ which is more than the 8.1 kJ required to power a SOLO-II float for a 10-day cycle. At 0.4 Ω, the electrical energy generated is 13.66 kJ, which is more than one and a half times the energy requirement for a

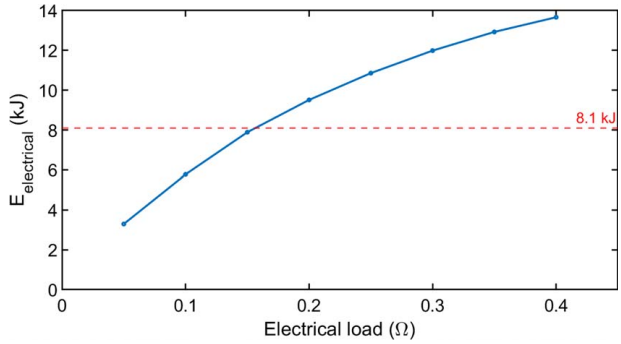

Fig. 4 Electrical energy generated with different resistive loads with $P_{initial} = 29$ MPa and $P_{max} = 41.37$ MPa inside the hydraulic accumulator

SOLO-II float for a profiling cycle. In comparison, the OTEC-PCM [18] with 6 kg of PCM generated 6.696 kJ of electrical energy. As stated previously, a maximum value of 0.4 Ω is used in the simulation because beyond 0.4 Ω the instantaneous power generated by the DC motor exceeds its nominal power, due to less torque in the electrical generator and excessive rotational speed. In practice, when the power becomes excessive and beyond the generator's specifications, the dynamic and electrical losses become highly nonlinear; therefore, in this model, the simulation is performed within the motor's specifications.

At the maximum load of 0.4 Ω using Eqs. (14), (15), and (1), the calculated hydraulic-to-kinetic, kinetic-to-electric, and total energy conversion efficiencies are 73.76%, 69.2%, and 51.04% respectively. The increase of the energy conversion efficiencies compared to the values used from Ref. [18], is due primarily to the high pressure of the system modeled here. Even though an AC motor or brushless DC motor can be more efficient, long-lasting, and suitable for high electrical power applications, the choice of a DC generator reduces the electrical losses in an AC voltage rectifier. Additionally, a mechanical gearbox is avoided in this model to reduce mechanical losses but may be needed practically to match the hydraulic and the electric motors' torque. Matching the torque of both motors is needed for good efficiency.

Figure 5 shows the evolution of the pressure and hydraulic oil volume inside the accumulator with the pressure source activated. The pressure starts to build up rapidly from the initial N_2 gas precharge pressure of 29 MPa (4218.84 psi) until it reaches a value of ~41.4 MPa (6000 psi), after which the pressure stays constant. It is important to note that in Fig. 5, the unit of the calculated pressure is in absolute pressure. At the same time, the volume of oil increases rapidly from 0 s to 5 s, then accumulates more slowly until it reaches a maximum volume of 0.778 L (47.47 in.^{3}). The difference between the simulated value and the calculated value of 0.78 L (47.6 in.^{3}) is due to the leakage permitted by MATLAB/SIMULINK in components such as the pressure relief valve.

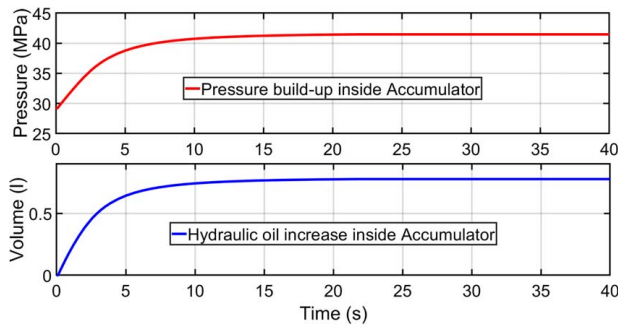

Fig. 5 Evolution of pressure and transfer fluid volume inside the 1-gallon nominal size accumulator during the hydraulic energy buildup phase

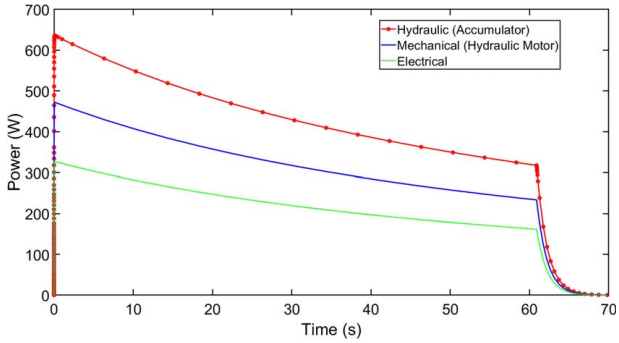

Fig. 6 Power delivered by the accumulator, hydraulic motor, and electrical generator with the electrical load value = 0.4 Ω

As described in Sec. 3.2, after pressure buildup inside the accumulator, a signal is given to open the solenoid valve, after which the pressurized fluid flows through the hydraulic motor which rotates an electrical generator to generate electricity, which is dissipated through the resistive load. Figure 6 shows the hydraulic power delivered by the accumulator, the kinetic power from the hydraulic motor, and the electrical power at 0.4 Ω resistive load. Initially, after the solenoid valve is opened, the power values reach a maximum within seconds, then decrease slowly as the fluid flows through the hydraulic motor to the hydraulic reservoir. The time for power generation, from the opening to closing of the solenoid valve is 60.8 s at 0.4 Ω, excluding the time for energy storage in the accumulator, which has been set to 40 s in the simulation (Fig. 5), using the solenoid valve opening signal (SO in Fig. 3). The solenoid valve is closed during the 40 s hydraulic energy storage in the accumulator and opened after 40 s to let flow the pressurized hydraulic oil through the hydraulic motor. It is important to note that in practical application, the oil flow in the accumulator will be different and depend on the melting rate of the PCM, when a thermal engine containing a PCM is used. The maximum torque and speed of the generator, when the electrical load is 0.4 Ω, are 2.4317 N·m and 1853.4 rpm, respectively. The power generation time increases with decreasing resistance values. For instance, at 0.05 Ω, the power generation time is 114.8 s. This is due to the torque increase from the electrical generator as the load values decrease. The corresponding maximum torque and rotational speed values of the generator at 0.05 Ω are 2.435 N·m and 727.37 rpm, respectively. As shown in Fig. 6, the maximum hydraulic, kinetic, and electrical power values at 0.4 Ω after the solenoid valve opens are 650.7 W, 471.9 W, and 326.2 W, respectively. After opening the solenoid valve to let flow the hydraulic oil from the accumulator, the hydraulic power flow through the hydraulic motor, the kinetic energy generated by the hydraulic motor, and the electrical energy generated by the DC motor instantly reach a maximum value. The power values decrease as the oil continues flowing through the hydraulic motor. Once all the oil from the accumulator has flown out, the energy conversion process stops, and the instantaneous power values drop to zero. For example, in Fig. 6, when the electrical load value is 0.4 Ω, the energy conversion process lasts for ~61 s. When all the oil flows through the hydraulic motor, it stops rotating and afterward, the power values drop to zero. The difference between the power values from the accumulator and the hydraulic motor is due mainly to the mechanical and volumetric losses inside the hydraulic motor, which decrease the power output of the hydraulic motor compared to the accumulator. Similarly, the difference between the power values from the hydraulic motor and the electrical generator is due mainly to the electrical (armature resistance) and mechanical losses (rotor damping) of the generator.

It should be noted that for practical applications, system inherent losses such as mechanical vibrations of the system, impurities, and air solubility within the PCM and hydraulic oil, hydraulic motor internal leakages, pipe leakages, and electrical generator losses should be minimized. A high-power brushless AC motor could replace the DC motor for long-term operations and efficient electrical generation. Moreover, a power management system with maximum efficiency point tracking algorithms [39], or maximum power point tracking [40] may be added to the system to minimize losses and increase the overall system efficiency. Furthermore, a thermal engine that can efficiently harvest the ocean thermal energy and quickly melt/solidify the quantity of PCM calculated for this model will be beneficial for practical applications.

5 Conclusion

A simplified numerical and computational model of a PCM-based thermal ocean energy harvester is proposed to simulate and optimize its electrical energy generation. The model targets the energy requirement for a profiling cycle of the SOLO-II float used by the Argo program. The simulated model shows that with 5.73 kg of hexadecane, 13.66 kJ of electrical energy per cycle can be generated with an optimal electrical load of 0.4 Ω, which is more than one and a half times the energy requirement per cycle of a SOLO-II float. This work will guide engineers in the development and optimization of PCM-based ocean thermal energy harvesters for independently powering the SOLO-II platform, as well as spread the use of this technology to other ocean-faring platforms such as gliders, and mobile underwater power stations.

Acknowledgment

This research was supported in part by an appointment with Marine and Hydrokinetic Graduate Student Research Program sponsored by the US Department of Energy (DOE), Office of Energy Efficiency and Renewable Energy, and Water Power Technologies Office (WPTO). This program is administered by the Oak Ridge Institute for Science and Education (ORISE) for the DOE. ORISE is managed by ORAU under DOE contract number DESC0014664.

All opinions expressed in this paper are the author's and do not necessarily reflect the policies and views of DOE, ORAU, or ORISE.

Conceptual design and ongoing laboratory experiments are conducted as a part of WPTO's Powering the Blue Economy Initiative.

Conflict of Interest

There are no conflicts of interest.

Data Availability Statement

The datasets generated and supporting the findings of this article are obtainable from the corresponding author upon reasonable request.

Nomenclature

i = electrical current (A)
m = mass (kg)
n = polytropic index
q = volumetric flowrate (m^3/s)
t = time (s)
v = back-emf (V)
E = energy (J)
K = Hagen–Poiseuille's coefficient
P = pressure (Pa)
R = electrical resistance (Ω)
V = volume (m^3)
k_t = torque constant
k_v = back-emf constant
N_2 = nitrogen

T_0 = start time (s)
T_f = final time (s)
ΔP = pressure difference (Pa)
ΔV = volume difference (m^3)

Greek Symbols

η = energy conversion efficiency
ρ = density (kg/m^3)
τ = torque ($N \cdot m$)
ω = angular velocity (rad/s)

Subscripts

m = hydraulic motor
G = gas
avg = average
max = maximum
Acc = accumulator

Abbreviations

OTEC = ocean thermal energy conversion
PCM = phase change material
SOLO = sounding oceanographic Lagrangian observer
UUV = uncrewed underwater vehicle

References

[1] Thomalla, S. J., Nicholson, S.-A., Ryan-Keogh, T. J., and Smith, M. E., 2023, "Widespread Changes in Southern Ocean Phytoplankton Blooms Linked to Climate Drivers," Nat. Clim. Change, **13**(9), pp. 975–984.
[2] Petersen, S., Krätschell, A., Augustin, N., Jamieson, J., Hein, J. R., and Hannington, M. D., 2016, "News From the Seabed—Geological Characteristics and Resource Potential of Deep-Sea Mineral Resources," Mar. Pol., **70**, pp. 175–187.
[3] Zhang, S., 2011, "Impact of Observation-Optimized Model Parameters on Decadal Predictions: Simulation With a Simple Pycnocline Prediction Model," Geophys. Res. Lett., **38**(2).
[4] Hotaling, Liesl, and Spinrad, Richard W., 2021, "Exploration and Technology—Key Building Blocks for the New Blue Economy," *Preparing a Workforce for the New Blue Economy: People, Products and Policies*, 1st ed., Elsevier, New York, pp. 3–16.
[5] Cisneros-Montemayor, A. M., Moreno-Báez, M., Reygondeau, G., Cheung, W. W. L., Crosman, K. M., González-Espinosa, P. C., Lam, V. W. Y., et al., 2021, "Enabling Conditions for an Equitable and Sustainable Blue Economy," Nature, **591**(7850), pp. 396–401.
[6] Su, F., Fan, R., Yan, F., Meadows, M., Lyne, V., Hu, P., Song, X., et al., 2023, "Widespread Global Disparities Between Modelled and Observed Mid-Depth Ocean Currents," Nat. Commun., **14**(1), p. 2089.
[7] Le Traon, P.-Y., D'Ortenzio, F., Babin, M., Leymarie, E., Marec, C., Pouliquen, S., Thierry, V., et al., 2020, "Preparing the New Phase of Argo: Scientific Achievements of the NAOS Project," Front. Mar. Sci., **7**, p. 577408.
[8] Whitt, C., Pearlman, J., Polagye, B., Caimi, F., Muller-Karger, F., Copping, A., Spence, H., et al., 2020, "Future Vision for Autonomous Ocean Observations," Front. Mar. Sci., **7**, p. 697.
[9] Wang, G., Yang, Y., and Wang, S., 2020, "Ocean Thermal Energy Application Technologies for Unmanned Underwater Vehicles: A Comprehensive Review," Appl. Energy, **278**, p. 115752.
[10] Crimmins, D. M., Patty, C. T., Beliard, M. A., Baker, J., Jalbert, J. C., Komerska, R. J., Chappell, S. G., and Blidberg, D. R., 2006, "Long-Endurance Test Results of the Solar-Powered AUV System," OCEANS 2006, Boston, MA, Sept. 18–21, pp. 1–5.
[11] Zhao, T., Xu, M., Xiao, X., Ma, Y., Li, Z., and Wang, Z. L., 2021, "Recent Progress in Blue Energy Harvesting for Powering Distributed Sensors in Ocean," Nano Energy, **88**, p. 106199.
[12] Ahmadi, P., Dincer, I., and Rosen, M. A., 2015, "Performance Assessment of a Novel Solar and Ocean Thermal Energy Conversion Based Multigeneration System for Coastal Areas," ASME J. Sol. Energy Eng., **137**(1), p. 011013.
[13] Arunachalam, S., 2019, "Latent Heat Storage: Container Geometry, Enhancement Techniques, and Applications—A Review," ASME J. Sol. Energy Eng., **141**(5), p. 050801.
[14] Messenger, M. A., Troxler, C. J., Melendez, I., Freeman, T. B., Reed, N., Rodriguez, R. M., and Boetcher, S. K. S., 2023, "Mechanical and Thermal Characterization of Phase-Change Material and High-Density Polyethylene Functional Composites for Thermal Energy Storage," ASME J. Sol. Energy Eng., **145**(6), p. 061006.
[15] Elavarasan, R. M., Singh, P., Leoponraj, S., Khanna, S., and Chandran, M., 2022, "Solar Photovoltaics Integrated With Hydrated Salt-Based Phase Change Material," ASME J. Sol. Energy Eng., **144**(5), p. 051004.
[16] Webb, D. C., Simonetti, P. J., and Jones, C. P., 2001, "SLOCUM: An Underwater Glider Propelled by Environmental Energy," IEEE J. Oceanic Eng., **26**(4), pp. 447–452.
[17] Xia, Q., Muhammad, G., Chen, B., Zhang, F., Zhang, Z., Zhang, S., and Yang, C., 2021, "Investigation of Self-Driven Profiler With Buoyancy Adjusting System Towards Ocean Thermal Energy," Appl. Sci., **11**(15), p. 7086.
[18] Wang, G., Yang, Y., Wang, S., Zhang, H., and Wang, Y., 2019, "Efficiency Analysis and Experimental Validation of the Ocean Thermal Energy Conversion With Phase Change Material for Underwater Vehicle," Appl. Energy, **248**, pp. 475–488.
[19] Chao, Y., 2016, "Autonomous Underwater Vehicles and Sensors Powered by Ocean Thermal Energy," Oceans 2016, Shanghai, China, Apr. 10–13, pp. 16–19.
[20] Zhang, H., Ma, X., and Yang, Y., 2022, "An External Ocean Thermal Energy Power Generation Modular Device for Powering Smart Float," Energies, **15**(10), pp. 3747.
[21] Haldeman, C. D., Schofield, O., Webb, D. C., Valdez, T. I., and Jones, J. A., 2015, "Implementation of Energy Harvesting System for Powering Thermal Gliders for Long Duration Ocean Research," OCEANS 2015, Washington DC, Oct. 19–22, pp. 1–5.
[22] Ma, Z., Wang, Y., Wang, S., and Yang, Y., 2016, "Ocean Thermal Energy Harvesting With Phase Change Material for Underwater Glider," Appl. Energy, **178**, pp. 557–566.
[23] Wang, G., Yang, Y., and Wang, S., 2022, "Thermophysical Properties Analysis of Graphene-Added Phase Change Materials and Evaluation of Enhanced Heat Transfer Effect in Underwater Thermal Vehicles," J. Mol. Liq., **348**, p. 118048.
[24] Wang, G., Yang, Y., Wang, S., Zhang, H., and Wang, Y., 2020, "Modification of the Phase Change Transfer Model for Underwater Vehicles: A Molecular Dynamics Approach," Int. J. Energy Res., **44**(14), pp. 11323–11344.
[25] Stommel, H., 1989, "The Slocum Mission," Oceanography, **2**(1), pp. 22–25.
[26] Jung, H., Subban, C. V., McTigue, J. D., Martinez, J. J., Copping, A. E., Osorio, J., Liu, J., and Deng, Z. D., 2022, "Extracting Energy From Ocean Thermal and Salinity Gradients to Power Unmanned Underwater Vehicles: State of the Art, Current Limitations, and Future Outlook," Renewable Sustainable Energy Rev., **160**, p. 112283.
[27] Morris, T., Scanderbeg, M., West-Mack, D., Gourcuff, C., Poffa, N., Bhaskar, T. V. S. U., Hanstein, C., et al., 2024, "Best Practices for Core Argo Floats—Part 1: Getting Started and Data Considerations," Front. Mar. Sci., **11**, p. 1358042.
[28] Bruvik, E. E., Fer, I., Väge, K., and Haugan, P. M., 2020, "A Revised Ocean Glider Concept to Realize Stommel's Vision and Supplement Argo Floats," Ocean Sci., **16**(2), pp. 291–305.
[29] Roemmich, D., Sherman, J. T., Davis, R. E., Grindley, K., McClune, M., Parker, C. J., Black, D. N., et al., 2019, "Deep SOLO: A Full-Depth Profiling Float for the Argo Program," J. Atmos. Oceanic Technol., **36**(10), pp. 1967–1981.
[30] Yang, Y., Wang, Y., Ma, Z., and Wang, S., 2016, "A Thermal Engine for Underwater Glider Driven by Ocean Thermal Energy," Appl. Therm. Eng., **99**, pp. 455–464.
[31] Liu, T., Sha, H., Li, M., Sun, M., Chen, G., Jiang, D., and Song, Y., 2022, "Theoretical Analyses on a Piston-Based Thermal Engine for Thermal Underwater Glider," Appl. Therm. Eng., **213**, p. 118718.
[32] Leon-Quiroga, J., Newell, B., Krishnamurthy, M., Gonzalez-Mancera, A., and Garcia-Bravo, J., 2020, "Energy Efficiency Comparison of Hydraulic Accumulators and Ultracapacitors," Energies, **13**(7), p. 1632.
[33] Accumulators, Inc., "Available Models—Bladder Accumulators," https://www.accumulators.com/bladder-accumulators/available-models/#1489519840336-83650bcf-2f7b.
[34] Chen, Y., Chen, B., He, M., Zhang, L., Xia, Q., and Yang, C., 2022, "Performance Study of Energy Conversion System for Ocean Thermal Profiler," Front. Mar. Sci., **9**, p. 996204.
[35] Hou, H., Arredondo Galeana, A., Song, Y., Xu, G., Xu, Y., and Shi, W., 2023, "Design of a Novel Energy Harvesting Mechanism for Underwater Gliders Using Thermal Buoyancy Engines," Ocean Eng., **278**, p. 114310.
[36] Sliwinski, P., and Patrosz, P., 2021, "The Influence of Water and Mineral Oil on Pressure Losses in Hydraulic Motor," Advances in Hydraulic and Pneumatic Drives and Control 2020. NSHP 2020. Lecture Notes in Mechanical Engineering, J. Stryczek, and U. Warzyńska, eds., Springer, Cham.
[37] MathWorks, "Fixed-Displacement Motor (IL)," https://www.mathworks.com/help/hydro/ref/fixeddisplacementmotoril.html.
[38] MathWorks, "DC Motor," https://www.mathworks.com/help/sps/ref/dcmotor.html.
[39] Xia, Q., Chen, Y., Yang, C., Chen, B., Muhammad, G., and Ma, X., 2020, "Maximum Efficiency Point Tracking for an Ocean Thermal Energy Harvesting System," Int. J. Energy Res., **44**(4), pp. 2693–2703.
[40] Benadli, R., Frey, D., Lembeye, Y., Bjaoui, M., Khiari, B., and Sellami, A., 2023, "A Direct Backstepping Super-Twisting Algorithm Controller MPPT for a Standalone Photovoltaic Storage System: Design and Real-Time Implementation," ASME J. Sol. Energy Eng., **145**(6), p. 061002.